

Constructing Rich Crystalline–Amorphous Heterojunction In NiCoMo/Ag Composites for High-Performance Supercapacitor

Qing Pang, Tengfei Wang, Boyu Liu, and Hongyu Wang*

The crystalline–amorphous heterojunction (C–AH) has become an important strategy for constructing electrode materials due to the synergistic effect between the high conductivity from the crystalline phase and the fast ion transport capabilities from the amorphous phase. In this work, a NiCoMo/Ag_x (NCM/Ag_x) electrode material with abundant C–AH interfaces is successfully produced on nickel foam substrates through a facile one-step hydrothermal approach. The optimized NCM/Ag_x electrode demonstrates good

electrochemical performance, delivering an areal capacitance of 9266.7 mF cm⁻² (125.23 mAh g⁻¹) at 2 mA cm⁻² and retaining 84.7% rate capability at 10 mA cm⁻². It is combined with activated carbon to construct an asymmetric supercapacitor, which achieves an energy density of 55.13 Wh kg⁻¹ at a power density of 750 W kg⁻¹, while also demonstrating a capacity retention of 79.7% after 10 000 cycles. This research supplies a theoretical basis for the design of high-performance supercapacitors.

1. Introduction

At present, the increasingly intensified global energy crisis and environmental degradation make it an urgent task to develop advanced energy storage systems to meet the surging energy demand.^[1–3] Among new energy storage technologies, supercapacitors occupy an important position in the realm of electrochemical energy storage, forasmuch to their good power density, fast charging–discharging rates, and simple preparation process.^[4] However, their lower energy density is a problem that cannot be ignored in supercapacitors. According to the energy density formula, which is closely related to the specific capacity of electrode materials,^[5] Therefore, preparing high-performance electrode materials has become the current research focus.

Transition metal compounds (especially Ni/Co/Mo-based oxides) are favored by researchers because of their substantial theoretical specific capacitance and rich ion synergistic effects.^[6,7] However, the actual energy density of transition metal compounds is lower than the theoretical energy density due to their low electrical conductivity. To solve this problem, researchers have explored strategies such as doping,^[8,9] defect engineering,^[10] and combining them with carbon-based materials or other pseudocapacitive materials.^[11–13] At present, most of the transition metal compounds mainly concerned are crystalline electrode materials. Crystalline electrode materials have the

advantage of high conductivity.^[14] However, the insertion and removal of ions during the cycling process, crystalline electrode materials are prone to pulverization, which affects their cycle stability.^[15] Compared with crystalline electrode materials, amorphous electrode materials have a weak impact due to their disordered structure.^[16,17] However, amorphous electrode materials have poor conductivity. Therefore, compounding crystalline materials with amorphous materials can make up for the shortcomings of both. It can enhance the charge transfer path, improve conductivity, and maintain structural stability. For example: Tu et al.^[18] synthesized crystalline TiN through a hydrothermal approach, followed by the preparation of amorphous NiMnO_x on the surface of TiN through another hydrothermal process and thermal treatment, ultimately obtaining a crystalline–amorphous heterojunction (C–AH) electrode material. This electrode exhibited a remarkable specific capacitance of 4882 mF cm⁻² at 5 mA cm⁻² and retained 63.4% rate capability at 40 mA cm⁻². The electrochemical performance is enhanced owing to the C–AH structure of the electrode material. Hou et al.^[19] synthesized crystalline NiWO₄ nanorods via a hydrothermal method, followed by depositing amorphous Co–B on their surface through chemical deposition, thereby obtaining C–AH (NiWO₄/Co–B). Electrochemical performance evaluations demonstrated a specific capacitance of 304 F g⁻¹ at 0.5 A g⁻¹, and retaining 69% rate capability at 10 A g⁻¹. After 10 000 cycles, it retained 90.8% capacitance. The excellent electrochemical performance stems from the synergistic effect between crystalline NiWO₄ and amorphous Co–B, which efficiently enhances ion diffusion and electron transport throughout the charge–discharge process. Karthik et al.^[20] synthesized crystalline MnMoO₄ through chemical deposition and high-temperature calcination, followed by the synthesis of amorphous Ni_xB on the surface of crystalline MnMoO₄ via chemical deposition, thereby obtaining the C–AH electrode material (Ni_xB/MnMoO₄). Experimental

Q. Pang, T. Wang, B. Liu, H. Wang

Qinghai Provincial Key Laboratory of New Light Alloys

Qinghai Provincial Engineering Research Center of High-Performance Light Metal Alloys and Forming

Qinghai University

Xining 810016, P.R.China

E-mail: wanghongyu@qhu.edu.cn



Supporting information for this article is available on the WWW under <https://doi.org/10.1002/batt.202500368>

results showed that the prepared electrode exhibited high reversibility and good performance. The specific capacitance of 587.4 F g^{-1} at 1 A g^{-1} . After 5000 cycles, the capacity retention rate was 92.27%. The good electrochemical performance is due to the interaction between the rapid ion transport channels of amorphous Ni_xB and the high conductivity of crystalline MnMoO_4 . Although the construction of C-AH electrode materials can significantly enhance the conductivity of amorphous materials, most researchers combine them with crystalline metal compounds, which still exhibit a certain gap in conductivity compared to pure metals. Moreover, most researchers synthesize C-AH electrode materials through a two-step method. Therefore, there are fewer heterojunction interfaces present. Rich C-AH interfaces can regulate the electron density at the interface sites and promote charge transfer,^[21] thus can contribute to the high performance of electrode materials.

Silver (Ag) is one of the materials with the best conductivity.^[22,23] Compounding with it can effectively ameliorate the conductivity of the amorphous material. Furthermore, by choosing the synthesis process, both crystalline and amorphous phases can be generated simultaneously, resulting in the distribution

of crystalline materials within the amorphous materials, thereby achieving rich C-AH interfaces.

Based on this, this research proposes a novel one-step reduction deposition strategy and successfully constructs a high-performance supercapacitor electrode material with rich C-AH interfaces ($\text{NiCoMo}/\text{Ag}_1$). The introduction of Ag not only significantly improves the conductivity of the NCM matrix but also promotes the coexistence of crystalline and amorphous phases and forms rich C-AH interfaces. The optimized $\text{NiCoMo}/\text{Ag}_1$ (NCM/Ag_1) electrode exhibits a specific capacitance of $9266.67 \text{ mF cm}^{-2}$ ($125.23 \text{ mAh g}^{-1}$) at 2 mA cm^{-2} and retains 74.02% of its capacity after 10 000 cycles. This work offers a theoretical basis for the design of supercapacitor heterojunction interfaces.

2. Results and Discussion

2.1. Structure Characterization

Figure 1a illustrates the synthesis mechanism of the rich C-AH interface electrode material (NCM/Ag_1). Under hydrothermal

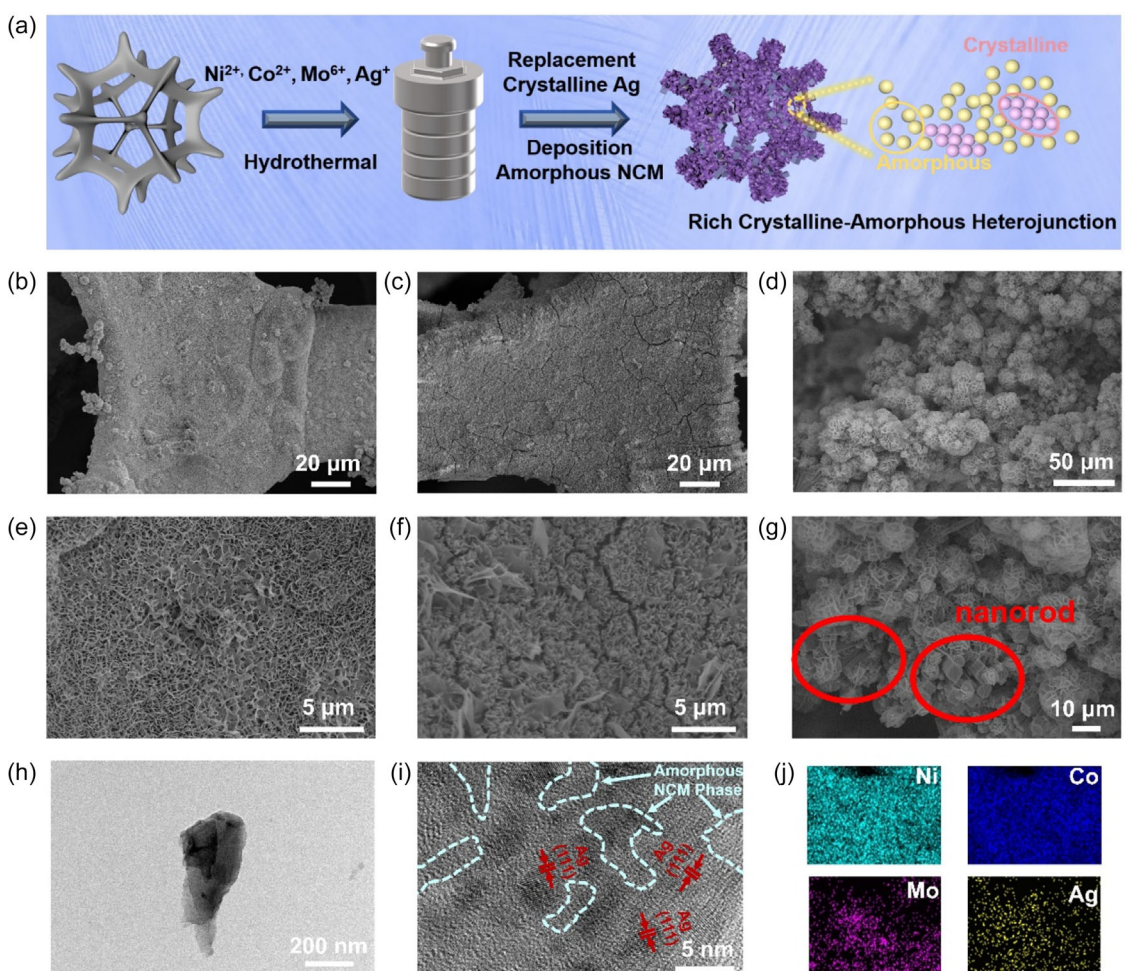


Figure 1. a) Preparation process diagram of NCM/Ag_1 , b and e) SEM images of NC, c and f) NCM, d and g) NCM/Ag_1 , h and i) TEM images, and j) EDS images of NCM/Ag_1 .

conditions, the Ag^+ ions in the solution undergo a substitution reaction with nickel foam (NF) (reaction formula: $2\text{Ag}^+ + \text{Ni} \rightarrow 2\text{Ag} + \text{Ni}^{2+}$ ^[21]), thereby promoting the formation of crystalline Ag. Simultaneously, the reaction releases Ni^{2+} ions, which combine with Co^{2+} and Mo^{6+} to form the amorphous NCM phase. Thus, the crystalline Ag/amorphous NCM heterojunction electrode material was constructed. The amorphous NCM phase provides rich unsaturated coordination sites and shortened ion diffusion pathways, while the crystalline Ag ensures efficient electron transfer. The synthesized rich C-AH interface electrode material optimizes the charge transfer kinetics and improves the electrochemical performance through the synergistic effect of these two phases.^[24]

Figure S1, Supporting Information shows the scanning electron microscopy (SEM) images of NF, and its surface is smooth. Compared with NF, the surfaces of NC, NCM, and NCM/ Ag_1 are all loaded with active electrode materials. The surface of NC is uniformly covered with nanosheets (Figure 1b,e). After the addition of Mo, the morphology of the sample remains a sheet-like structure, but the size is significantly smaller compared to NC (Figure 1c,f), primarily because the Mo element facilitates the refinement of the structure, leading to changes in material size.^[9] When Ag is further introduced, the nanosheet structure disappears, forming a composite structure of tremella-like and nanorods (Figure 1d,g). Additionally, the mass loading of NCM/ Ag_1 (11.1 mg cm^{-2}) exceeds that of NC (3.9 mg cm^{-2}) and NCM (9 mg cm^{-2}). This indicates that Ag promotes the transformation of amorphous NCM into tremella-like and nanorod structures and increases the sample loading capacity. To investigate how Ag content affects morphology and performance, samples containing 0.5 mmol (NCM/ $\text{Ag}_{0.5}$) and 1.5 mmol (NCM/ $\text{Ag}_{1.5}$) were also prepared and characterized (Figure S2, Supporting Information). All samples containing Ag exhibited a morphology characterized by the coexistence of tremella-like structures and nanorods, with the number of nanorods increasing as the Ag content rose: NCM/ $\text{Ag}_{0.5}$ showed fewer nanorods (loading capacity of 10.7 mg cm^{-2}); NCM/ $\text{Ag}_{1.5}$ demonstrated an increased number of nanorod structures (loading capacity of 9.8 mg cm^{-2}). By adjusting the hydrothermal time (2–8 h), the morphological evolution can be observed (Figure S3, Supporting Information): NCM/ $\text{Ag}_{1.2}$ (2 h) is mainly in the form of nanorods and presents a sea urchin-like structure (loading 8.8 mg cm^{-2}); when extended to 4 h, the sea urchin-like structure gradually changes into tremella-like structure, but the size is smaller (loading 10.3 mg cm^{-2}); after 6 h, it is completely transformed into tremella-like structure, and reaches the maximum size. At 8 h, the size is smaller (loading 12.5 mg cm^{-2}). It can be seen that the formation of a tremella-like structure is directly related to the hydrothermal process; a small amount of Ni^{2+} involved in the formation of NCM contributes to the generation of tremella-like structures, while an excessive amount of Ni^{2+} involved in the formation of NCM facilitates the generation of nanorod structures. The primary reason for this phenomenon is likely the difference in the relative content of Ni in the two morphologies of NCM, leading to the formation of different morphologies.

The transmission electron microscopy (TEM) image depicted in Figure S4, Supporting Information indicates that both NC and NCM are composed of nanosheets (aligning with the SEM findings), while the selected area electron diffraction (SAED) confirms their amorphous characteristics. While NCM/Ag₁ exhibits a composite structure of nanosheets and nanorods (Figure 1h,i, and S5, Supporting Information), the crystalline Ag is distributed in the amorphous NCM matrix, thus forming rich C-AH interfaces. This unique structure stems from the synchronous occurrence of replacement and deposition reactions during the synthesis process, thus proving that the rich C-AH electrode material has been successfully prepared. At the same time, energy dispersive spectroscopy (EDS) spectra (Figure 1j) confirm that the material contains four elements, Ni, Co, Mo, and Ag, and they are evenly distributed. To further explore the composition of the nanorods, an EDS analysis was conducted. The results showed that this structure is mainly composed of amorphous NCM (Figure S5, Supporting Information). This may be due to the addition of Ag, which promotes the formation of a rod-like structure of part of NCM.

Figure 2a shows the X-ray diffraction (XRD) spectra of NC, NCM, and NCM/Ag₁. NC and NCM only show the Ni diffraction peaks of the NF substrate ($2\theta = 44.494^\circ$, 51.847° , and 76.377° , corresponding to the (111), (200), and (220) crystal planes of Ni, JCPDS 04-003–3918), indicating that the active substance is amorphous or the loading amount is low. Combined with the TEM results, it is confirmed to be an amorphous structure. The Ag characteristic peaks (38.115° , 64.445° , and 77.399° , corresponding to the (111), (220), and (311) crystal planes of Ag, with JCPDS 03-065–2871) appearing in NCM/Ag₁ confirm the successful introduction of crystalline Ag. As the amount of Ag rises, the diffraction peak intensity of Ag is enhanced (Figure S6, Supporting Information), indicating that the relative content of Ag is increasing.

To analyze the valence states of elements on the surface of the synthesized electrode materials, X-ray photoelectron spectroscopy (XPS) analysis was conducted. The XPS survey spectrum in Figure 2b indicates the presence of Ni and Co signals in the NC material. The Mo signal was detected in the NCM sample, confirming the successful introduction of Mo. Additionally, the Ag signal was detected in the NCM/Ag₁ sample, demonstrating the successful incorporation of crystalline Ag, consistent with the XRD results. Figure 2c-f presents the detailed spectra of the three-electrode materials. The spectrum of Ni 2p (Figure 2c) exhibits the distinctive peaks associated with Ni^{2+} , which can be deconvoluted into $\text{Ni}^{2+} 2\text{p}_{3/2}$ at 856.3 eV , $\text{Ni}^{2+} 2\text{p}_{1/2}$ at 874.0 eV , and two satellite peaks (862.4 eV , 880.0 eV).^[25] In the Co 2p spectrum (Figure 2d), 781.2 eV ($\text{Co}^{2+} 2\text{p}_{3/2}$) and 796.9 eV ($\text{Co}^{2+} 2\text{p}_{1/2}$) are the main peaks, and the satellite peaks are located at 786.5 and 803.1 eV .^[25] The Mo 3d spectrum (Figure 2e) indicates that Mo exists in the form of Mo^{6+} ($3\text{d}_{5/2}$: 231.6 eV and $3\text{d}_{3/2}$: 234.8 eV).^[26] The Ag 3d spectrum (Figure 2f) shows the Ag 3d_{5/2} (368.3 eV) and Ag 3d_{3/2} (374.3 eV) peaks,^[27] confirming the existence of crystalline Ag.

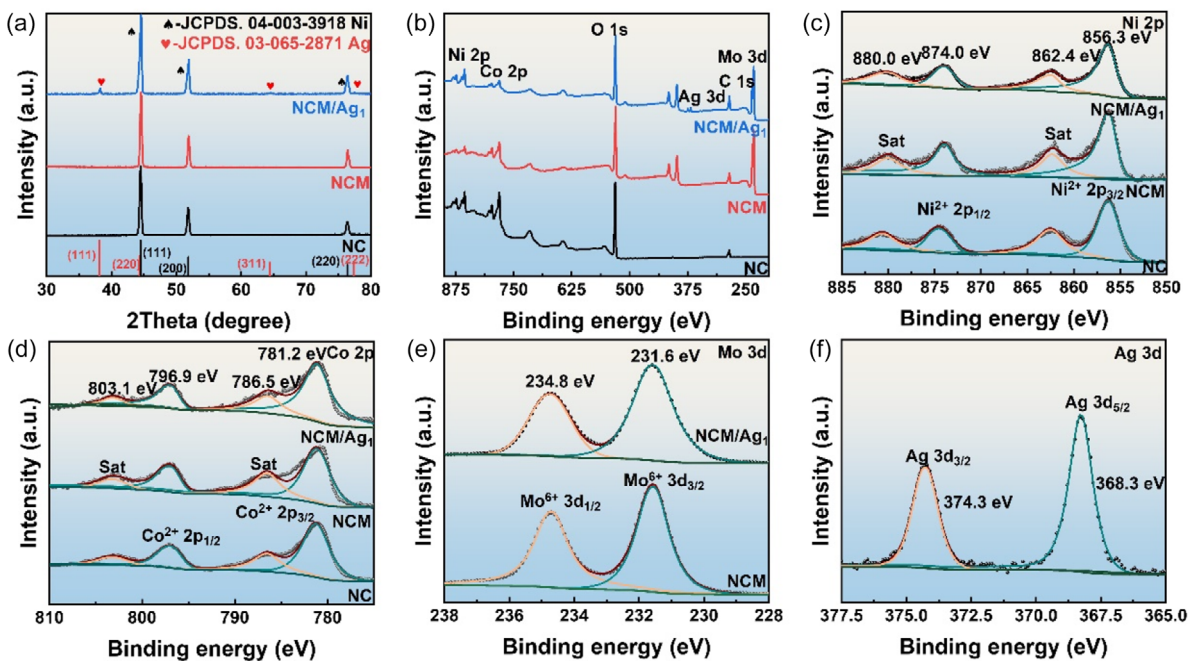


Figure 2. a) X-ray diffraction (XRD) patterns, b) overall survey spectrum, high-resolution spectra of c) Ni 2p, d) Co 2p, e) Mo 3d, and f) Ag 3d of NC, NCM, and NCM/Ag₁.

2.2. Electrochemical Characterization

The evaluation of the electrochemical characteristics for NC, NCM, and NCM/Ag₁ was conducted utilizing a three-electrode arrangement. Comparing the cyclic voltammetry (CV) curves (Figure 3a) of the three-electrode materials at 5 mV s⁻¹. The clear redox peaks can be ascribed to reversible Faraday reactions, thereby validating the electrochemical behavior typical of battery-type materials. And NCM/Ag₁ showed the largest integral area. Figure 3b illustrates the CV curves of NCM/Ag₁ at various scan rates. As the scan rate increases, the area under the CV curve enlarges, signifying an enhancement in electrochemical activity at elevated scanning rates. The peaks observed around 0.3 V (reduction peak) and 0.4 V (oxidation peak) are associated with the Faraday reaction of OH⁻ with Ni, Co, and Mo species in the alkaline electrolyte. The reaction equations are.^[28,29] Notably, NCM/Ag₁ displays an additional reduction peak at 0.2 V compared to NC and NCM, which originates from the successful incorporation of crystalline Ag. The corresponding redox reactions are expressed as^[30]

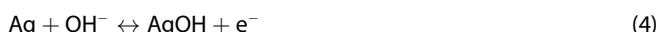
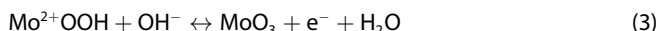
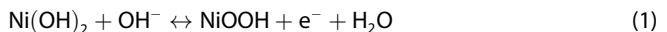


Figure 3c compares the galvanostatic charge–discharge (GCD) curves of NC, NCM, and NCM/Ag₁ at 2 mA cm⁻². The nearly symmetric charge–discharge curves indicate that it has a battery-type

energy storage behavior. NCM/Ag₁ has the longest discharge time, which proves that this electrode material has good capacity. To enhance the understanding of the electrochemical properties of electrode materials, one can calculate the specific capacity utilizing Equation S1, Supporting Information.^[31] The specific capacitances corresponding to the three-electrode materials are NC (2499.3 mF cm⁻²/96.13 mAh g⁻¹), NCM (6074.07 mF cm⁻²/101.23 mAh g⁻¹), and NCM/Ag₁ (9266.67 mF cm⁻²/125.23 mAh g⁻¹), respectively. This excellent performance stems from the rich C–AH interface between crystalline Ag and amorphous NCM in NCM/Ag₁, where crystalline Ag enhances conductivity, while amorphous NCM provides sufficient active sites. The synergistic effect enables the NCM/Ag₁ electrode material to have good electrochemical performance. Figure 3d shows the GCD curves of NCM/Ag₁ at different current densities. NCM/Ag₁ can retain 84.7% rate capability at 10 mA cm⁻². And the corresponding capacity retention rates of NC and NCM are 68.6% and 80.13% at 10 mA cm⁻² (Figure S7, Supporting Information). This indicates that the abundance of C–AH is beneficial for enhancing the rate performance of the sample. As shown in Figure S8, Supporting Information, the specific capacitance of NCM/Ag_{0.5} and NCM/Ag_{1.5} at 2 mA cm⁻² is 8792.59 mF cm⁻² (123.26 mAh g⁻¹) and 6703.7 mF cm⁻² (102.61 mAh g⁻¹), respectively. The specific capacitance exhibits an initial increase followed by a subsequent decrease as the Ag content rises. This trend can be attributed to the gradual increase in C–AH with higher Ag content; however, an excess of Ag can lead to an increase in amorphous NCM nanorods, ultimately resulting in diminished electrochemical performance. NCM/Ag₁ has more C–AH interfaces, so the electrochemical performance is the best. The specific capacitances of NCM/Ag_{1–2} and NCM/Ag_{1–4} at 2 mA cm⁻² are 6153 mF cm⁻² (104 mAh g⁻¹) and 8555.56 mF cm⁻²

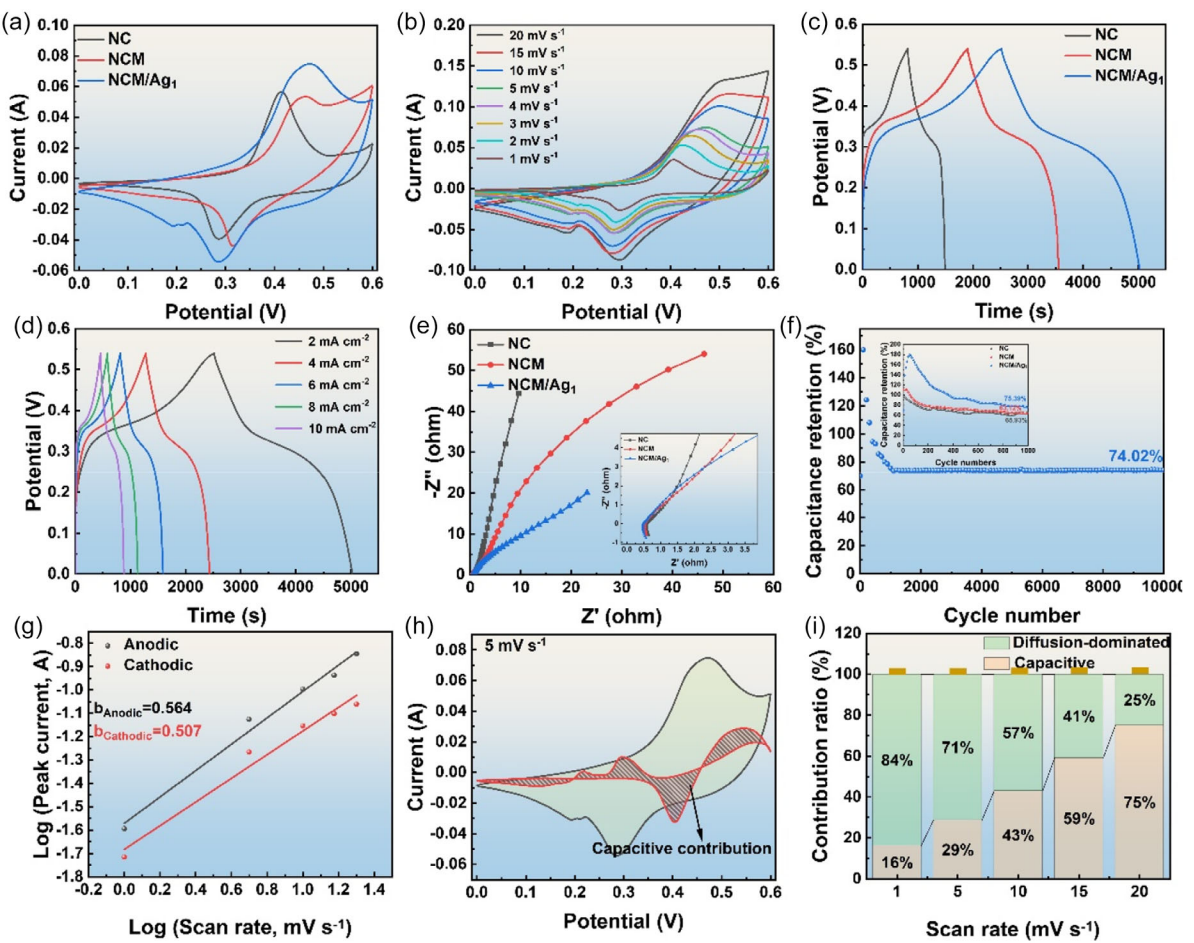


Figure 3. a) CCV curves of different electrodes recorded at a scan rate of 10 mV s⁻¹, b) CV curves of NCM/Ag₁ at different scan rates, c) GCD curves of different electrodes recorded at a current density of 2 mA cm⁻², d) GCD curves of NCM/Ag₁ at different current densities, e) Nyquist plots of different electrodes recorded, f) cycle performance diagram of different electrodes recorded, g) *b*-value determination for cathodic and anodic peaks, h) CV curve (shaded area) at 5 mV s⁻¹ demonstrating the capacitive and diffusion contributions, and i) corresponding bar diagram for capacitive/diffusion contribution ratios of NCM/Ag₁.

(124.59 mAh g⁻¹) (Figure S9, Supporting Information). It can be observed that as the hydrothermal time increases, the size of the tremella-like structure also increases, thereby fully contacting the electrolyte, and consequently, the discharge time gradually increases. When the hydrothermal time was increased to 8 h, the specific capacitance reached 10,680 mF cm⁻² (111.55 mAh g⁻¹) at 2 mA cm⁻², but the voltage window decreased to 0–0.47 V (Figure S9, Supporting Information). This is because an excessively long hydrothermal time reduces the size of the tremella-like structure, thereby diminishing the electrochemical performance.

Figure 3e shows the Nyquist plot of NC, NCM, and NCM/Ag₁. The series resistances (R_s) of the three are 0.59, 0.54, and 0.48 Ω, respectively, and the charge transfer resistances (R_{ct}) are 1.10, 1.01, and 0.96 Ω, respectively. This is attributed to its abundant crystalline Ag/amorphous NCM heterojunction structure, which significantly improves conductivity and optimizes ion/electron transport. For the two samples of NCM/Ag_{0.5}, NCM/Ag_{1.5}, the R_s values are 0.54 and 0.58 Ω, and the R_{ct} values are 1.21 and 1.58 Ω. This is related to the quantity of C-AH. For the three

samples of NCM/Ag_{1–2}, NCM/Ag_{1–4}, and NCM/Ag_{1–8}, the R_s values are 0.57, 0.55, and 0.53 Ω, respectively, and the R_{ct} values are 1.20, 1.11, and 1.06 Ω (Figure S10, Supporting Information). This is closely related to the size of the tremella-like structure. Figure 3f compares the cycling performance of NC, NCM, and NCM/Ag₁. After 1000 cycles, the capacity retention rates are NC (65.93%), NCM (63.12%), and NCM/Ag₁ (75.39%), respectively. Notably, both NCM and NCM/Ag₁ exhibit a phenomenon where capacity initially increases and then decreases during the first 100 cycles. The initial increase is due to electrode activation, and the subsequent decrease is due to excessive loading leading to a weak bonding force between the active material and the current collector, resulting in shedding. After the partial active material shedding in the first 100 cycles, no active material shedding occurred in the subsequent cycles. Therefore, after 10 000 cycles, the capacity retention rate of NCM/Ag₁ is 74.02%. It indicates that the introduction of Ag significantly improves the cycling stability. The synergistic effect of the C-AH enables NCM/Ag₁ to have the best comprehensive performance. The electrochemical

performance of NCM/Ag₁ was compared with that of reported C-AH electrode materials, and it was found that NCM/Ag₁ had good electrochemical performance (Table S1, Supporting Information).

The charge storage mechanism was analyzed using Equation S2, Supporting Information.^[32] The *b* values recorded for the anode and cathode peaks of NCM/Ag₁ are 0.564 and 0.507, respectively (Figure 3g), confirming that its charge storage mechanism is mainly capacitive-controlled. A quantitative analysis via Eq. S3.^[33] The results show that the diffusion process dominates at 5 mV s⁻¹ (Figure 3h). When the scanning rate increases from 1 to 20 mV s⁻¹, the capacitance contribution of NCM/Ag₁ increases from 16% to 75% (Figure 3i). The increase in the capacitance contribution of NCM/Ag₁ is due to the high conductivity of Ag, expediting the charge transfer kinetics, highlighting the advantages of the C-AH compared to the pure amorphous system.

After 10 000 cycles, the characterization and analysis of NCM/Ag₁ were conducted using XRD, SEM, TEM, and XPS techniques. The XRD pattern shows that the phase remains unchanged after

cycling (Figure 4a). The XPS full spectrum confirms that Ni, Co, Mo, and Ag still exist in the material (Figure 4b), but the Co 2p and Mo 3d signals decay significantly. The Ni 2p valence state is consistent with the original state (Figure 4c). While Co exists in the form of Co³⁺, the main peaks are 781.1 eV (Co³⁺ 2p_{3/2}) and 796.5 eV (Co³⁺ 2p_{1/2}), and the satellite peaks are located at 798.8 and 805.0 eV.^[34] There are two forms of Mo⁶⁺ and Mo⁴⁺. Mo⁴⁺ 3d_{5/2} and Mo⁶⁺ 3d_{3/2} are respectively in 228.8 eV and 235.7 eV (Figure 4d-e).^[35] The energy loss peak of Ag 3d appears at 376.8 eV (Figure 4f). These changes originate from the redox reactions occurring on the surface during cycling. SEM shows that the nanorods completely disappear after cycling, and the tremella-like structure partially collapses, but the overall framework is retained (Figure 4g-h). TEM shows that the crystalline Ag/amorphous NCM heterojunction structure still exists after cycling (Figure 4i), and EDS verifies the uniform distribution of each element (Figure 4j). In summary, the NCM/Ag₁ electrode material demonstrates a degree of structural stability.

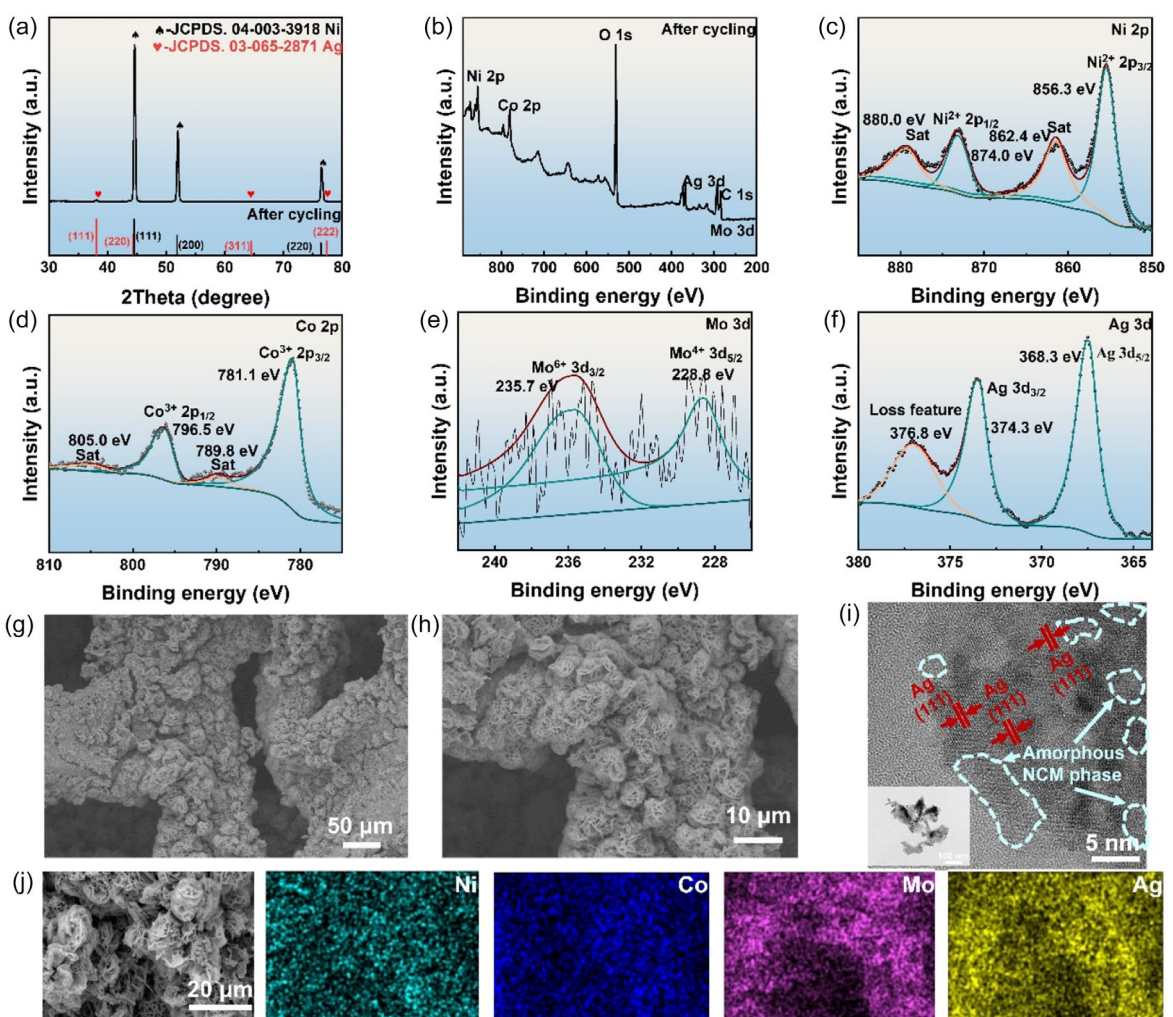


Figure 4. a) XRD patterns, b)overall survey spectrum, high-resolution spectra of c) Ni 2p, d) Co 2p, e) Mo 3d, and f) Ag 3d, g–h) SEM images, i) TEM image, and j) EDS images of NCM/Ag₁ after cycling.

2.3. Electrochemical Characterization of ASC and SS

To verify the application potential of NCM/Ag₁, it was assembled with activated carbon (AC) into an NCM/Ag₁//AC asymmetric supercapacitor (ASC) (Figure 5a). Figure 5b compares the CV curves of NCM/Ag₁ and AC at 20 mV s⁻¹. The voltage range for NCM/Ag₁ is between 0 and 0.6 V, whereas for AC it spans from -1 to 0 V. As shown in Figure 5c, exceeding this window (>1.5 V) will trigger the oxygen evolution reaction, resulting in a sharp increase in current density. Figure 5d shows that the device exhibits battery behavior at 10–50 mV s⁻¹, and the CV curve still maintains good reversibility at high scanning rates. The Nyquist plot indicates that the ohmic resistance of the device is $R_s = 0.56$ and $R_{ct} = 0.66 \Omega$ (Figure 5e). Moreover, the specific capacitance of this device is 176.4 F g⁻¹ at 1 A g⁻¹, and retaining 60.7% rate capability at 5 A g⁻¹. In order to gain a clearer insight into the device's electrochemical performance, one can compute the respective energy density and power density using Equation S4 and S5, Supporting information.^[36] Its energy density can reach 55.13 Wh kg⁻¹ at 750 W kg⁻¹ (Figure 5g). After 10 000 cycles

of charge and discharge, it still has 79.7% of its capacity. And by connecting two devices in series, an LED bulb can be lit, operating for 27 min (Figure 5h). Compared with the reported devices, the performance of NCM/Ag₁//AC is significantly better than that of NiCoMn//rGO,^[37] Ni₃S₄QDs@ZIN-P//AC,^[38] NCM-S@HCNS//3D N-rGO,^[39] and Ni₂P@C//AC^[40] (Figure 5i).

Figure S11, Supporting Information presents the electrochemical performance of the symmetric device NCM/Ag₁//NCM/Ag₁. The operating voltage range is between 0 and 0.6 V, with R_s measuring 0.68 Ω and R_{ct} at 0.76 Ω. The device has a specific capacity of 376 F g⁻¹ at 3 A g⁻¹, and an energy density of 18.8 at 900 W kg⁻¹. Its performance is better than that of the symmetric supercapacitors.^[41–46]

The excellent performance of the device stems from its key structural advantage—rich C-AH interfaces (Figure 6). The composite structure formed by crystalline Ag and amorphous NCM creates rich C-AH interfaces, enhancing the interfacial conductivity and ion transport path. It also promotes charge transfer by regulating the electron density of interface sites.

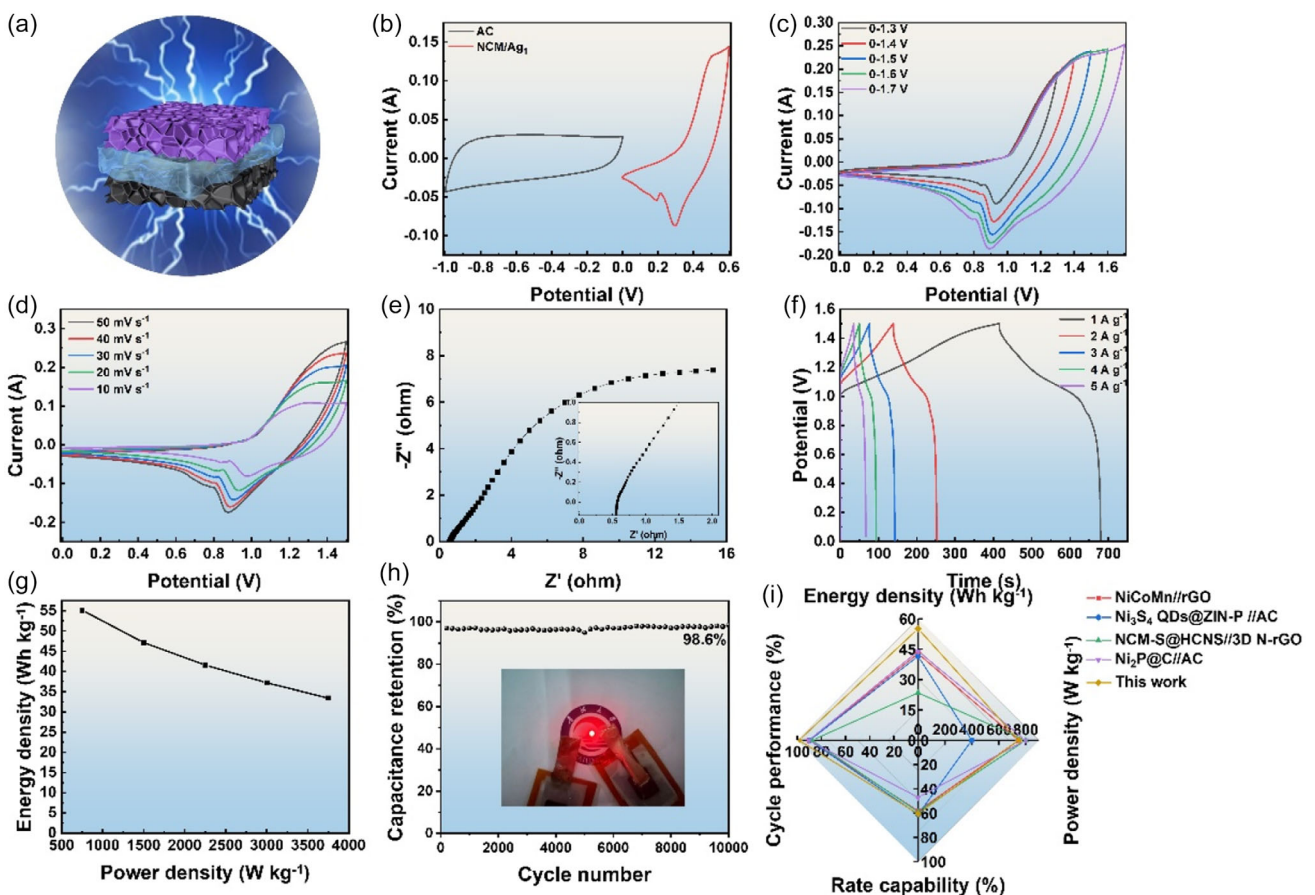


Figure 5. a) Schematic illustration, b) CV curves of AC and NCM/Ag₁, c) CV curves in different potential windows, d) CV curves at different scan rates, e) Nyquist plots, f) GCD curves at different current densities, g) Ragone diagram, h) cyclic stability, and i) electrochemical performance comparison diagram of ASC.

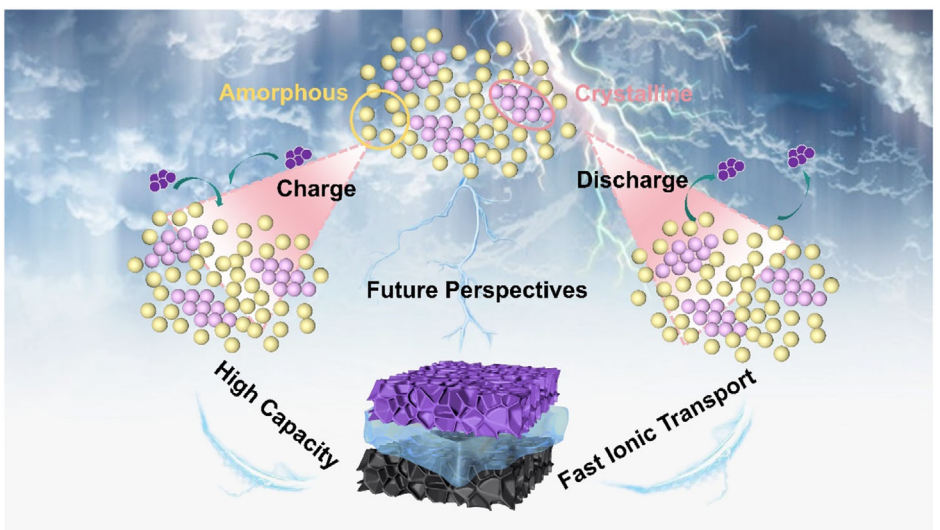


Figure 6. Performance advantage diagram of NCM/Ag₁.

3. Conclusion

In summary, we successfully synthesized a rich C-AH electrode material (crystalline Ag/amorphous NCM) through a straightforward one-step hydrothermal approach. Systematic studies revealed the critical roles of hydrothermal duration and Ag content in governing morphological evolution and electrochemical performance. The synergistic effects of C-AH endow NCM/Ag₁ with an areal capacitance of 9266.67 mF cm⁻² (125.23 mAh g⁻¹) at 2 mA cm⁻² and retain 74.02% capacity after 10 000 cycles. The constructed NCM/Ag₁/AC attains an energy density of 55.13 Wh kg⁻¹ at 750 W kg⁻¹. This research offers a reference for the development of high-performance supercapacitors.

4. Experimental Section

Materials

The following chemicals were procured from commercial suppliers: cobalt source ($\text{Co}(\text{NO}_3)_2 \cdot 6\text{H}_2\text{O}$), molybdenum source ($(\text{NH}_4)_6\text{Mo}_7\text{O}_{24} \cdot 4\text{H}_2\text{O}$), and silver salt (AgNO_3) from Sinopharm Co., Ltd. KOH (electrolyte) was supplied by Shanghai McLean Biochemical Co., while NF substrate was acquired from Changde Liyuan Material Co. All materials were of analytical purity.

Synthesis of C-AH of NiCoMo/Ag (NCM/Ag)

The NCM/Ag₁ composite was synthesized via a single-step hydrothermal method. Before synthesis, NF substrates underwent sequential ultrasonication in hydrochloric acid (3 M), deionized water, and ethanol. A homogeneous solution containing stoichiometric amounts of $\text{Co}(\text{NO}_3)_2 \cdot 6\text{H}_2\text{O}$ (0.49 mmol), ammonium $(\text{NH}_4)_6\text{Mo}_7\text{O}_{24} \cdot 4\text{H}_2\text{O}$ (0.07 mmol), and AgNO_3 (0.1 mmol) in 15 mL deionized water was prepared and transferred to a Teflon-lined autoclave. After 5 min of ultrasonic dispersion, the hydrothermal process was conducted at 150 °C for 6 h. The resultant product was alternately rinsed with deionized water and ethanol, followed by drying at 60 °C for a duration of 12 h. This procedure has been documented in previous studies.^[21]

And NC, NCM, NCM/Ag_{0.5} (0.05 mmol AgNO_3), and NCM/Ag_{1.5} (0.15 mmol AgNO_3) were fabricated using identical procedures. Additionally, time-dependent samples (NCM/Ag₁₋₂, NCM/Ag₁₋₄, and NCM/Ag₁₋₈) were obtained by modulating hydrothermal durations to 2, 4, and 8 h, respectively.

Characterization

The crystallographic characteristics were examined utilizing a D-max2500 PC X-ray diffractometer (XRD) that employs Cu K α radiation ($\lambda = 1.5406 \text{ \AA}$). The scan was conducted within the range of 30° to 80° at a steady speed of 3° per minute. Morphological traits were investigated using SU8010 SEM and JSM-IT210 TEM. The chemical state was analyzed using an X-ray photoelectron spectrometer (XPS, ESCALABX), applying charge correction where the binding energy of C 1s is set at 284.8 eV as the energy reference.

The electrochemical characteristics were evaluated with a CHI760E workstation configured in a three-electrode arrangement, utilizing a 6 M KOH electrolyte under ambient conditions. The configuration included a working electrode made of NCM/Ag, a counter electrode composed of Pt, and a reference electrode that was a saturated calomel. Various techniques were employed, including CV, ranging from 0 to 0.6 V, GCD, between 2 and 10 mA cm⁻², and electrochemical impedance spectroscopy (EIS, spanning 0.01–10⁵ Hz).

Assembly of an Asymmetric Supercapacitor (ASC) and a Symmetric Supercapacitor (SS)

ASCs were constructed with NCM/Ag₁ (positive) and activated carbon (AC, negative) electrodes, while symmetric devices (SS) utilized dual NCM/Ag₁ electrodes. A gel electrolyte comprising 1 M KOH and 1 g polyvinyl alcohol was uniformly applied.

Supporting Information

The Supporting Information is available free of charge at the Calculation formula of areal specific capacitance (C_s), b value, energy density (E), and power density (P). SEM images, TEM

images, EDS, XRD patterns, CV curves, GCD curves, Nyquist plots, *b* value, and corresponding bar diagram for capacitive/diffusion contribution ratios of other electrode materials. And the electrochemical performance of the symmetric device NCM/Ag₁//NCM/Ag₁.

Acknowledgements

The authors gratefully acknowledge the financial support by the program of Science and Technology of Qinghai Province (no. 2024-ZJ-761).

Conflict of Interest

The authors declares no conflicts of interest.

Author Contributions

Qing Pang: writing—original draft; methodology; investigation.
Tengfei Wang: methodology; investigation.
Boyu Liu: methodology; investigation.
Hongyu Wang: writing—review & editing; supervision; conceptualization.

Data Availability Statement

The data that support the findings of this study are available from the corresponding author upon reasonable request.

Keywords: electrochemical properties • electrode materials • NiCoMo/Ag₁ • rich crystalline–amorphous heterojunction • supercapacitors

- [1] L. Liu, Z. Li, H. Wang, *Electrochim. Acta* **2023**, *441*, 141819.
- [2] L. Zhang, F. Fan, X. Song, W. Cai, J. Ren, H. Yang, N. Bao, *J. Materomics* **2024**, *10*, 348.
- [3] W.-J. Liu, M. Yuan, J.-B. Lian, G.-C. Li, Q.-P. Li, F. Qiao, Y. Zhao, *Tungsten* **2023**, *5*, 118.
- [4] L. Liu, S. Zuo, H. Wang, *Acs Appl. Nano Mater.* **2024**, *7*, 15903.
- [5] Y. Chen, Y. Li, Y. Dong, D. Li, S. Shen, J. Hu, Y. Fu, D. He, J. Li, *Sci. China Mater.* **2024**, *67*, 816.
- [6] Q. Zhang, G. Wang, T. Chen, H. Wu, R. Yuan, B. Ai, P. Liang, D. Fang, Q. Min, *New J. Chem.* **2023**, *47*, 21865.
- [7] J. Li, D. Pan, P. Xu, J. Liang, S. Luo, C. Hu, *Nano Energy* **2024**, *128*, 109954.
- [8] X. Huang, B. Chu, B. Han, Q. Wu, T. Yang, X. Xu, F. Wang, B. Li, *Small* **2024**, *20*, 2401315.
- [9] S. Xiong, S. Weng, Y. Tang, L. Qian, Y. Xu, X. Li, H. Lin, Y. Xu, Y. Jiao, J. Chen, *J. Colloid Interface Sci.* **2021**, *602*, 355.
- [10] C.-W. Luo, K. Zhang, H.-Y. Zeng, H.-B. Wang, K.-W. Xu, B. Feng, G.-Z. Wu, *J. Power Sources* **2025**, *633*, 236403.
- [11] L. Vivas, A. Jara, J. M. Garcia-Garfido, D. Serafini, D. P. Singh, *ACS Omega* **2022**, *7*, 42446.
- [12] S. Fu, J. Chen, X. Wang, Q. He, S. Tong, M. Wu, *Small* **2020**, *16*, 2000040.
- [13] Y. Zhou, L. Wei, C. Li, Y. Han, J. Xu, Z. Jia, J. Sun, H. Chen, Y. Song, X. Ouyang, *J. Energy Storage* **2022**, *45*, 103765.

- [14] L. Zhang, L. Dong, M. Li, P. Wang, J. Zhang, H. Lu, *J. Mater. Chem. A* **2018**, *6*, 1412.
- [15] J. Li, S. Luo, B. Zhang, J. Lu, W. Liu, Q. Zeng, J. Wan, X. Han, C. Hu, *Nano Energy* **2021**, *79*, 105410.
- [16] X. Ren, M. Li, L. Qiu, X. Guo, F. Tian, G. Han, W. Yang, Y. Yu, *J. Mater. Chem. A* **2023**, *11*, 5754.
- [17] X. Y. Li, X. J. Luo, D. S. Chen, L. X. Yang, H. Wang, T. Gao, Y. Liu, J. Lin, *Adv. Mater.* **2025**, *37*, 2417763.
- [18] H. Tu, D. Shi, Z. Liang, H. Jiang, Z. Kong, K. Zhang, Y. Shao, Y. Wu, X. Hao, *J. Mater. Chem. A* **2021**, *9*, 21948.
- [19] J. F. Hou, J. F. Gao, L. B. Kong, *Chem.—An Asian J.* **2021**, *16*, 4130.
- [20] R. Karthik, R. Sukanya, S. M. Chen, M. Hasan, G. Dhakal, P. M. Shafi, J.-J. Shim, *ACS Appl. Mater. Interfaces* **2023**, *15*, 11927.
- [21] D. Li, Y. Qin, J. Liu, H. Zhao, Z. Sun, G. Chen, D. Y. Wu, Y. Su, S. Ding, C. Xiao, *Adv. Funct. Mater.* **2022**, *32*, 2107056.
- [22] Z. Zhang, X. Li, C. Zhong, N. Zhao, Y. Deng, X. Han, W. Hu, *Angew. Chem. Int. Ed.* **2020**, *59*, 7245.
- [23] H. Sheng, X. Zhang, Y. Ma, P. Wang, J. Zhou, Q. Su, W. Lan, E. Xie, C. J. Zhang, *ACS Appl. Mater. Interfaces* **2019**, *11*, 8992.
- [24] X. Tang, J. Wang, D. Zhang, B. Wang, X. Xia, X. Meng, B. Yang, J. Chen, Y. He, Z. Han, *Chem. Eng. J.* **2023**, *452*, 139429.
- [25] J. Wang, L. Yang, Y. Fu, P. Yin, X. Guan, G. Wang, *Nanoscale* **2021**, *13*, 8562.
- [26] Y. Gao, J. Tao, J. Li, H. Xie, Y. Li, T. Wang, C. Zhang, *J. Alloys Compd.* **2022**, *925*, 166705.
- [27] X. Wu, Y. Qiu, W. Cai, J. Li, D. Wu, L. Xu, Y. Kong, *Chem. Eng. J.* **2024**, *484*, 149667.
- [28] K. A. Owusu, Z. Wang, A. Saad, F. O. Boakye, M. A. Mushtaq, M. Tahir, G. Yasin, D. Liu, Z. Peng, X. Cai, *Energy Environ. Mater.s* **2024**, *7*, e12545.
- [29] G. Manibalan, Y. Govindaraj, J. Yesuraj, P. Kuppusami, G. Murugadoss, R. Murugavel, M. R. Kumar, *J. Colloid Interface Sci.* **2021**, *585*, 505.
- [30] M. Zhao, Q. Zhao, J. Qiu, X. Lu, G. Zhang, H. Xue, H. Pang, *Part. Part. Syst. Charact.* **2017**, *34*, 1600412.
- [31] L. Liu, W. Lv, H. Wang, *J. Energy Storage* **2023**, *73*, 109062.
- [32] G. Maheshwaran, G. Seethalakshmi, V. K. Devi, L. M. VenkataKrishna, M. R. Prabhu, M. K. Kumar, S. Sudhahar, *Curr. Appl. Phys.* **2022**, *36*, 63.
- [33] U. Kurtan, H. Aydin, B. Büyük, U. Şahintürk, M. Almessiere, A. Baykal, *J. Energy Storage* **2020**, *32*, 101671.
- [34] Y.-C. Chen, S. Kubendhiran, R.-J. Chung, C. Kongvarhodom, S. Husain, S. Yougbaré, H.-M. Chen, Y.-F. Wu, L.-Y. Lin, *J. Energy Storage* **2025**, *112*, 115530.
- [35] Y. Zhao, S. Wang, M. Yuan, Y. Chen, Y. Huang, J. Lian, S. Yang, H. Li, L. Wu, *Chem. Eng. J.* **2021**, *417*, 127927.
- [36] Y. Wang, X. Li, Z. Huang, H. Wang, Z. Chen, J. Zhang, X. Zheng, Y. Deng, W. Hu, *Angew. Chem. Int. Ed.* **2023**, *62*, e202215256.
- [37] H. C. Chen, Y. Qin, H. Cao, X. Song, C. Huang, H. Feng, X. Zhao, *Energy Storage Mater.* **2019**, *17*, 194.
- [38] J. Zheng, X. Lian, M. Wu, F. Zheng, Y. Gao, H. Niu, *Colloids Surf., A* **2021**, *623*, 126710.
- [39] Y. Zhou, Z. Jia, S. Zhao, P. Chen, Y. Wang, T. Guo, L. Wei, X. Cui, X. Ouyang, X. Wang, *Chem. Eng. J.* **2021**, *416*, 129500.
- [40] F. Xu, Q. Xia, G. Du, Z. Fan, N. Chen, *Electrochim. Acta* **2021**, *380*, 138200.
- [41] Y. Wang, X. Wang, X. Li, R. Liu, Y. Bai, H. Xiao, Y. Liu, G. Yuan, *Nanomicro. Lett.* **2020**, *12*, 1.
- [42] I. M. Babu, M. Sureshkumar, R. Rajeshkumar, I. Rathinamala, *J. Alloys Compd.* **1010**, 2025, 177472.
- [43] U. Şahintürk, B. Üstün, H. Aydin, S. N. Koç, Ü. Kurtan, *J. Power Sources* **2024**, *613*, 234882.
- [44] R. Sankannavar, R. Bhosale, R. Kangutkar, S. Kolekar, J. Manjanna, *J. Energy Storage* **2024**, *94*, 112455.
- [45] D. Johnsirani, A. Pandurangan, *Diam. Relat. Mater.* **2020**, *105*, 107800.
- [46] F. B. Ajdari, M. D. Najafi, M. I. Ostad, H. R. Naderi, M. N. Shahrok, E. Kowsari, S. Ramakrishna, *J. Mol. Liq.* **2021**, *333*, 116007.

Manuscript received: May 14, 2025

Revised manuscript received: August 14, 2025

Version of record online: